

Two-dimensional transition metal chalcogenides with hexagonal and orthorhombic structures: candidates for auxetics and photocatalysts

Wenqi Xiong,¹ Kaixiang Huang,¹ and Shengjun Yuan^{1,*}

¹Key Laboratory of Artificial Micro- and Nano-structures of Ministry of Education and School of Physics and Technology, Wuhan University, Wuhan 430072, China

In this paper, we perform theoretical study on the physical properties of two-dimensional transition metal chalcogenides MX_2 and M_2X_3 ($\text{M} = \text{Ni}, \text{Pd}$; $\text{X} = \text{S}, \text{Se}, \text{Te}$). These studied materials are classified in three stable phases according to their lattice structures: hexagonal MX_2 , orthorhombic MX_2 and orthorhombic M_2X_3 . They have either isotropic or anisotropic in-plane properties depending on their symmetries. In particular, the orthorhombic MX_2 and M_2X_3 have low lattice symmetry and present highly anisotropic properties. The orthorhombic MX_2 possess giant negative in-plane Poisson's ratios, different from the other two phases. Moreover, by joint analysis of band gap, band edge and optical absorption, the orthorhombic MX_2 and M_2X_3 are found to be highly efficient as water splitting photocatalysts within the visible and ultraviolet sunlight regions.

PACS numbers: 62.20.Dc, 63.20.dk, 85.30.De

I. INTRODUCTION

Two-dimensional (2D) group-VIII transition metal chalcogenides (TMCs), including the transition metal dichalcogenides (for example, MoS_2 , MoSe_2 , WS_2 and WSe_2 , etc.) have presented great potentials in electronic and optical devices, such as high current on/off ratio field-effect transistors (FETs) [1, 2], photodetectors [3, 4] and valleytronic applications [5, 6]. Most reported 2D TMCs have isotropic mechanical and electronic properties due to their highly symmetric structures. The symmetry of lattice structure indeed plays a vital role in determining the electronic properties of materials. By lowering the symmetry of the structure, it is possible to induce strong in-plane anisotropic properties in 2D materials, as observed in puckered phosphorene [7, 8] and group-IV monochalcogenides (SnS , SnSe , GeS , GeSe) [9–11]. As have already been reported, the anisotropic properties have the advantage for certain applications, such as polarized light detection devices and valleytronics [12–14].

Recently, few-layer PdSe_2 has been successfully synthesized via mechanical exfoliation and selenization on the precursor Pd layer [15–17], which has aroused great interests due to its ambient stability, high carrier mobility ($\sim 158 \text{ cm}^2\text{V}^{-1}\text{s}^{-1}$) and in-plane anisotropic properties [18]. In contrast to its hexagonal phase (Fig.1(b)), the synthesized few-layer PdSe_2 forms an orthorhombic lattice with puckered pentagonal structure as illustrated in Fig. 1(c). Moreover, Li *et al.* revealed a much lower diffusion barrier of Se vacancies in PdSe_2 than that of S vacancy in MoS_2 [19]. Further, Lin *et al.* demonstrated that the introduction of Se vacancy in few-layer PdSe_2 can enhance the interlayer interaction and decrease the Se/Pd element ratio, which creates a new structure phase, *i.e.*, Pd_2Se_3 [20], as shown in Fig. 1(d).

It is therefore highly desired to look for other 2D TMCs with a similar structure as PdSe_2 or Pd_2Se_3 , which may be stable and reveal the in-plane anisotropic properties.

Furthermore, one important application of 2D materials is the photocatalytic water splitting, *i.e.*, to convert solar energy into chemical energy without additional cost [21–23]. Since the discovery of TiO_2 as a photocatalyst in 1972 [24], more and more semiconductors have been proposed, including 2D semiconductors such as $\text{g-C}_3\text{N}_4$ and MoS_2 [25, 26]. Particularly, one or few-layers 2D semiconductors are indeed thin, with inherent merit as photocatalysts due to their extremely large specific surface area. In fact, an ideal photocatalyst should have two characters: (i) the band edge need to straddle both the reduction potential of H_2/H^+ (-4.44 eV at $\text{pH}=0$) and the oxidation potential of $\text{H}_2\text{O}/\text{O}_2$ (-5.67 eV at $\text{pH}=0$); (ii) an appropriate optical gap to guarantee the absorption of the solar light. Once satisfying the principle (i), the holes and electrons can drive both the oxidation and reduction reactions to generate O_2 and H_2 from aqueous solution. We will use these principles to look for possible photocatalysts from the 2D TMCs studied in this paper.

In this paper, we will perform systematic study on 2D TMCs based on the VIII-VIA compounds in the form of M_mX_n , where M refers to the elements Ni and Pd, and X represents S, Se and Te. We will calculate the physical properties of eighteen 2D TMCs from first principles by using density functional theory (DFT). The structures of these materials are classified in three phases, namely, the hexagonal MX_2 (H- MX_2), the orthorhombic MX_2 (O- MX_2) and the orthorhombic M_2X_3 (O- M_2X_3). In the following, We will first present the details of the numerical methods in Sec. II and show the main results in Sec. III, including stability, mechanical, electronic and optical properties of monolayer M_mX_n , and their potential applications in photocatalyst. Finally, we summarize our major findings In Sec. IV.

* s.yuan@whu.edu.cn

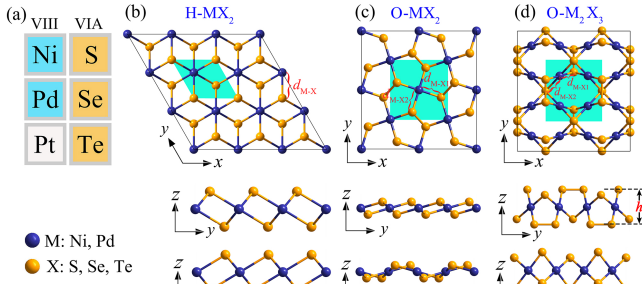


FIG. 1. (a) The VIII and VIA elements in periodic table. Top and side views of (b) H-MX₂, (c) O-MX₂ and (d) O-M₂X₃, respectively. The green regions denote the unit cell.

II. CALCULATION METHOD

The electronic properties of TMCs are calculated from first-principles by using DFT as implemented in VASP code [27]. The Perdew-Burke-Ernzerhof (PBE) parametrized generalized gradient approximation (GGA) and projected augmented wave (PAW) are adopted to describe exchange correlation potential and ion-electron interaction [28, 29]. The kinetic energy cutoff and k -point mesh of Brillouin zone (BZ) are set to 500 eV and $15 \times 15 \times 1$ [30], respectively. A vacuum thickness of 20 Å is added to avoid the periodic interaction. Moreover, the energy convergence criteria and stress forces are set to 10^{-5} eV and 0.01 eV/Å, respectively. For few-layer TMCs, the van der Waals (vdW) force is corrected by using a semi-empirical DFT-D2 method [31, 32]. The spin-orbit coupling (SOC) is added into self-consistent calculations. Also, the corrected band structures are calculated by adopting hybrid Heyd-Scuseria-Ernzerhof (HSE06) method [33].

The thermal stability of monolayer TMCs is evaluated by using PHONOPY code based on density functional perturbation theory (DFPT) and finite difference method [34–36]. We construct a 3×3 supercell and adopt $5 \times 5 \times 1$ k -point mesh to obtain force constants and phonon spectrum. In order to eliminate the imaginary frequency, the highly accurate energy convergence criteria and stress forces are set to 10^{-8} eV and 10^{-4} eV/Å, respectively.

III. RESULTS AND DISCUSSIONS

A. Structural stability

We firstly study the basic geometric structures and thermal stability of monolayer M_mX_n ($M = \text{Ni, Pd}$; $X = \text{S, Se, Te}$). After fully optimizing the atomic positions, the M_mX_n stabilizes into three structural symmetries as shown in Fig. 1, namely, the hexagonal H-MX₂, the orthorhombic O-MX₂, and the orthorhombic O-M₂X₃. All geometric structures are built up with three atomic layers as X-M-X, in which one M layer is sandwiched with

TABLE I. Calculated lattice constants (a and b), bond lengths (d_{M-X}), vertical heights (h) band gaps from PBE (E_{gap}^{PBE}) and HSE06 (E_{gap}^{HSE}) methods of monolayer TMCs.

| | a (Å) | b (Å) | d_{M-X} (Å) | h | E_{gap}^{PBE} (eV) | E_{gap}^{HSE} (eV) |
|-----------------------------------|---------|---------|---------------|-------|----------------------|----------------------|
| H-NiS ₂ | 3.348 | 3.348 | 2.258 | 2.330 | 0.61 | 1.10 |
| H-NiSe ₂ | 3.547 | 3.547 | 2.390 | 2.467 | 0.21 | 0.58 |
| H-NiTe ₂ | 3.787 | 3.787 | 2.576 | 2.721 | 0 | 0 |
| H-PdS ₂ | 3.548 | 3.548 | 2.395 | 2.480 | 1.27 | 1.80 |
| H-PdSe ₂ | 3.730 | 3.730 | 2.523 | 2.627 | 0.72 | 1.13 |
| H-PdTe ₂ | 4.026 | 4.026 | 2.701 | 2.756 | 0.26 | 0.52 |
| O-NiS ₂ | 5.215 | 5.326 | 2.172/2.182 | 1.149 | 0.82 | 2.40 |
| O-NiSe ₂ | 5.512 | 5.702 | 2.305/2.314 | 1.368 | 1.02 | 2.27 |
| O-NiTe ₂ | 5.955 | 6.261 | 2.489/2.498 | 1.552 | 0.95 | 1.89 |
| O-PdS ₂ | 5.472 | 5.571 | 2.328/2.339 | 1.267 | 1.18 | 2.14 |
| O-PdSe ₂ | 5.744 | 5.919 | 2.452/2.462 | 1.488 | 1.36 | 2.16 |
| O-PdTe ₂ | 6.146 | 6.439 | 2.625/2.631 | 1.693 | 1.27 | 1.90 |
| O-Ni ₂ S ₃ | 5.239 | 5.57 | 2.190/2.256 | 3.438 | 0.38 | 1.77 |
| O-Ni ₂ Se ₃ | 5.423 | 5.926 | 2.310/2.383 | 3.704 | 0.37 | 1.61 |
| O-Ni ₂ Te ₃ | 5.499 | 6.737 | 2.488/2.571 | 4.105 | 0.30 | 1.05 |
| O-Pd ₂ S ₃ | 5.773 | 5.907 | 2.341/2.427 | 3.582 | 0.45 | 1.50 |
| O-Pd ₂ Se ₃ | 5.976 | 6.114 | 2.455/2.539 | 3.842 | 0.42 | 1.39 |
| O-Pd ₂ Te ₃ | 6.122 | 6.608 | 2.622/2.696 | 4.228 | 0.60 | 1.24 |

two X layers. Each M atom binds six X atoms in H-MX₂ and four X atoms in O-MX₂ and O-M₂X₃. Detailed geometry analysis show that the space groups of H-MX₂, O-MX₂ and O-M₂X₃ are $P3m1$ (No. 164), $P2_1/c$ (No. 14) and $Pmnm$ (No. 59), respectively. In contrast to the common phase of hexagonal H-MX₂, the space groups of O-MX₂ and O-M₂X₃ have much lower symmetry.

The relaxed structural parameters, such as lattice constants (a and b), bond lengths (d_{M-X}), and vertical heights (h) are listed in Table 1. These results show clearly that when the atomic radius of element M (X) increases from Ni (S) to Pd (Te), all bond lengths within the same structural phase always increase. Comparing to the hexagonal structure of H-MX₂, the bond lengths in two orthorhombic O-MX₂ and O-M₂X₃ are more close to each other, but the height, defined as the out of plane distance between the top and bottom X sub-layers, are totally different. Furthermore, for O-MX₂ and O-M₂X₃ phases, there are diversity of in-plane lattice constants along different crystal lines, originating from the bond length difference between d_{M-X1} and d_{M-X2} , as illustrated in Fig. 1. These differences break further the geometry symmetry and induce subsequently anisotropic mechanical and optical properties, as we will explore in detail in the following.

The thermal stability of O-MX₂ and O-M₂X₃ is qualitatively examined by ab initio molecular dynamics simulations implemented in GULP [37, 38]. Here we skip the discussion of H-MX₂, as these common hexagonal structures have already been synthesized successfully [39–41].

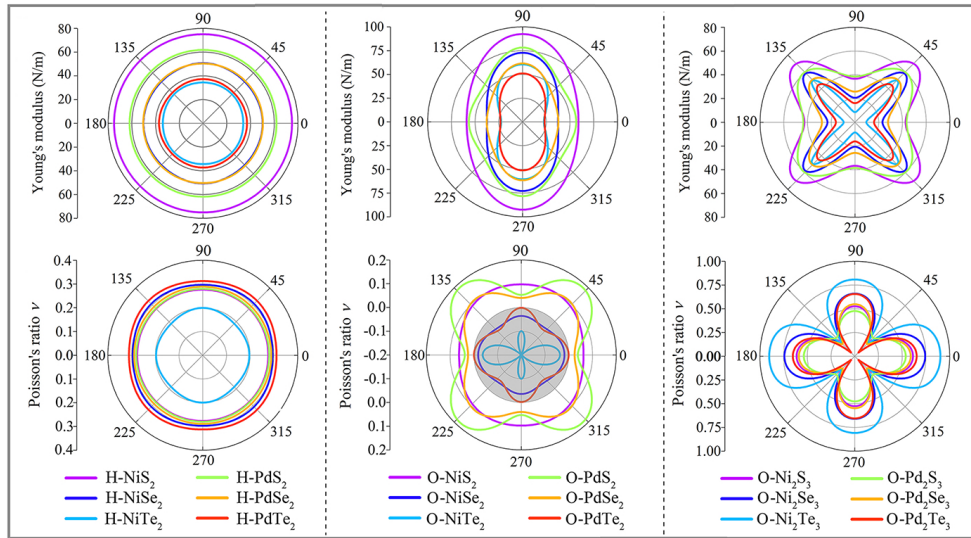


FIG. 2. Calculated orientation-dependent Young's modulus $Y(\theta)$ (top panel) and Poisson's ratio $v(\theta)$ (bottom panel) for H-MX₂, O-MX₂ and O-M₂X₃, respectively. The grey region denotes negative Poisson's ratio.

In our stability analysis, the 3×3 supercell of monolayer TMCs is used, the time interval and time step of the testing period are set to be 5×10^{-12} s and 1×10^{-15} s, respectively. Our results show that the total energy of each structure considered in the O-MX₂ and O-M₂X₃ phases is oscillating persistently around a fixed value during the whole simulation (see the data of 300K presented in Fig. S1 and S2 of Supplementary Information). The stability of these structures is further conformed from the spectra of phonon dispersions shown in Fig. S3 and Fig. S4 of Supplementary Information. No negative acoustic branch is observed for all the structures considered in this paper. These results obtained from ab initio molecular dynamics simulations and phonon dispersions from first-principles indicate that the monolayer O-MX₂ and O-M₂X₃ with M= Ni, Pd and X= S, Se, Te are all stable at room temperature. We will then continue the study by examining their mechanical and electronic properties, together with the phase of H-MX₂.

B. Mechanical properties

Three phases of monolayer TMCs considered in this paper present totally different lattice structures. Materials belonging to the same phase of TMCs may have similar properties originating from the characters of their space group, but these from different phases should have significant differences in their physical properties. As one of the most important mechanical properties, we examine first Young's modulus $Y(\theta)$ and Poisson's ratio $v(\theta)$ in the following.

Based on Hooke's law, the relationship between stiffness constants and modulus is given by

$$\begin{bmatrix} \sigma_{xx} \\ \sigma_{yy} \\ \sigma_{xy} \end{bmatrix} = \begin{bmatrix} C_{11} & C_{12} & 0 \\ C_{12} & C_{22} & 0 \\ 0 & 0 & C_{66} \end{bmatrix} \begin{bmatrix} \varepsilon_{xx} \\ \varepsilon_{yy} \\ 2\varepsilon_{xy} \end{bmatrix}, \quad (1)$$

where the in-plane stiffness tensor C_{ij} ($i, j=1, 2, 6$) is equal to the second partial derivative of strain energy E_s , which is obtained by

$$E_s = \frac{1}{2}C_{11}\varepsilon_{xx}^2 + \frac{1}{2}C_{22}\varepsilon_{yy}^2 + C_{12}\varepsilon_{xx}\varepsilon_{yy} + 2C_{66}\varepsilon_{xy}^2, \quad (2)$$

where the tensile strain is defined as $\varepsilon=(a-a_0)/a_0$, here a and a_0 are strained and unstrained lattice constants, respectively. Young's modulus Y and Poisson's ratio v can be expressed as functions of the in-plane stiffness tensors as[42]

$$Y_x = \frac{C_{11}C_{22} - C_{12}^2}{C_{22}}, \quad Y_y = \frac{C_{11}C_{22} - C_{12}^2}{C_{11}}, \quad (3)$$

$$v_x = \frac{C_{12}}{C_{22}}, \quad v_y = \frac{C_{12}}{C_{11}}, \quad (4)$$

In fact, the anisotropic mechanical feature can be further checked by calculating the orientation-dependent Young's modulus Y and Poisson's ratio v , which can be expressed as [43]

$$Y(\theta) = \frac{C_{11}C_{22} - C_{12}^2}{C_{11}s^4 + C_{22}c^4 + \left(\frac{C_{11}C_{22} - C_{12}^2}{C_{66}} - 2C_{12}\right)s^2c^2}, \quad (5)$$

$$v(\theta) = \frac{C_{12}(s^4 + c^4) - (C_{11} + C_{22} - \frac{C_{11}C_{22} - C_{12}^2}{C_{66}})s^2c^2}{C_{11}s^4 + C_{22}c^4 + \left(\frac{C_{11}C_{22} - C_{12}^2}{C_{66}} - 2C_{12}\right)s^2c^2}, \quad (6)$$

where $s=\sin\theta$ and $c=\cos\theta$.

The in-plane stiffness tensors C_{ij} are obtained from a series of strain $|\varepsilon| \leq 2\%$ and a step of 0.5%. All in-plane stiffness tensors C_{ij} fitting from Eq. (2) for eighteen monolayer TMCs are collected in Table S1 of Supplementary Information. The orientation-dependent Young's modulus $Y(\theta)$ and Poisson's ratio $\nu(\theta)$ calculated by using Eq. (5) and (6) are plotted in Fig. 2. It is clear that all structures in the H-MX₂ phase are isotropic as both Young's modulus $Y(\theta)$ and Poisson's ratio $\nu(\theta)$ keep as constants when varying θ ; but the other two phases, O-MX₂ and O-M₂X₃, are highly anisotropic with clear angle-dependent mechanical properties.

Particularly, Young's modulus of O-MX₂ phase increase monotonically from a minimum Young's modulus along x direction ($\theta=0^\circ$) to a maximum value along y direction ($\theta=90^\circ$). However, the maximum and minimum values of O-M₂X₃ phase are located at 45° and 0° (90°), respectively. For the same element M (*i.e.*, Ni, Pd), Young's modulus decreases as X changes from S to Te due to the increment of the M-X bond strength. Furthermore, our calculations show that O-Ni₂Te₃ and O-Pd₂Te₃ have ultra-low Young's modulus (< 20 N/m), which are even lower than monolayer graphene (340 N/m) and MoS₂ (125 N/m)[44, 45], indicating their enormous potential in flexible devices.

For Poisson's ratio, besides the quite interesting anisotropic feather appeared in O-MX₂ and O-M₂X₃, our calculations show that three monolayer TMCs, O-NiSe₂, O-NiTe₂ and O-PdTe₂, present negative Poisson's ratios. The absolute value of negative Poisson's ratio obtained among these materials is -0.228 in O-NiTe₂ along 56° to the x axis (see Fig. 1(c)). A material with negative Poisson's ratio exhibits an interesting auxetic effect, *i.e.*, it expands along one direction if stretched along another direction. Auxetic materials are highly desirable for tissue engineering, bulletproof vests and many other med-

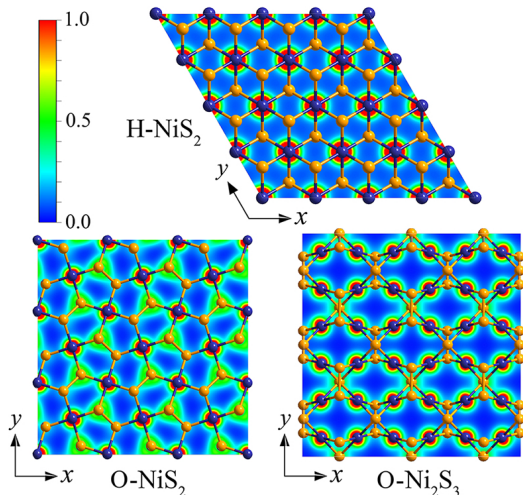


FIG. 3. The distribution of the charge density in the ground states of H-NiS₂, O-NiS₂ and O-Ni₂S₃. The color indicates the relative amplitude of the local densities.

TABLE II. The negative Poisson's ratios ν in x, y directions and its maximum values ν_{max} for other 2D materials.

| System | ν_x | ν_y | ν_{max} |
|-------------------------------------|---------|---------|-------------|
| O-NiSe ₂ | -0.018 | -0.036 | -0.050 |
| O-NiTe ₂ | -0.037 | -0.100 | -0.228 |
| O-PdTe ₂ | -0.001 | -0.002 | -0.058 |
| Borophene [42] | -0.022 | -0.009 | - |
| δ -Silica [46] | -0.123 | -0.112 | - |
| Penta-graphene [47] | -0.068 | -0.068 | - |
| Be ₅ C ₂ [48] | -0.041 | -0.16 | - |
| δ -AsN [49] | -0.177 | -0.068 | -0.296 |
| Tinselenidene [50] | -0.171 | 0.46 | - |

ical applications. As a comparison to existing auxetic 2D materials such as borophene, penta-graphene, tinselenidene, etc., we collect and list their Poisson's ratios together with current values of O-NiSe₂, O-NiTe₂ and O-PdTe₂ in Table 2. O-NiTe₂ has lowest Poisson's ratio among three studied materials, which is comparable to other reported auxetic 2D materials.

Actually, the nature of isotropic or anisotropic mechanical properties can be explained by analyzing the charge densities obtained from first principles. Here we use the case of M=Ni and X=S as an example to compare the charge distributions in three different structural phases. As plotted in Fig. 3, the charge densities of H-NiS₂ are localized isotropically around Ni atoms. On the contrary, the charge densities of O-NiS₂ and O-Ni₂S₃ are not uniformly distributed, but form patterns continuing along one crystal line. To be more precisely, for O-NiS₂, the extended pattern is along y direction, and for O-Ni₂S₃, it is along the diagonal direction. This is, indeed, consistent with the calculated Young's modulus, in which the maximum value appear along the continuous pattern. The electron orbitals are hybridized stronger along these directions, leading to larger overlap of wave functions and larger bonding strength, and subsequently higher stiffness.

C. Electronic properties

In this section, we study the electronic properties of monolayer TMCs. We firstly perform band structure calculations by using PBE. The results show that most materials considered in our paper are semiconductors (see details in Supplementary Information). As the PBE method usually underestimates the band gap of a semiconductor, we performed DFT calculations in VASP with more accurate HSE06 method and show the obtained band structures with projected densities in Fig. 4. The HSE06 results are similar as those in PBE, and all monolayer TMCs are semiconductors with indirect band gaps, except H-NiTe₂ which is a metal. Detailed analysis shows that, for H-MX₂ phase, the conduction

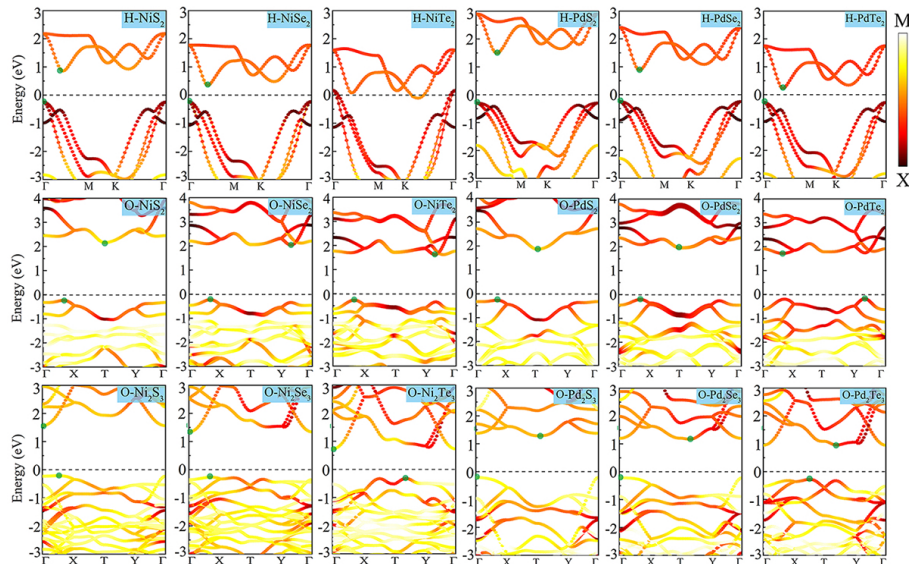


FIG. 4. The HSE06 projected band structures of eighteen monolayer TMCs.

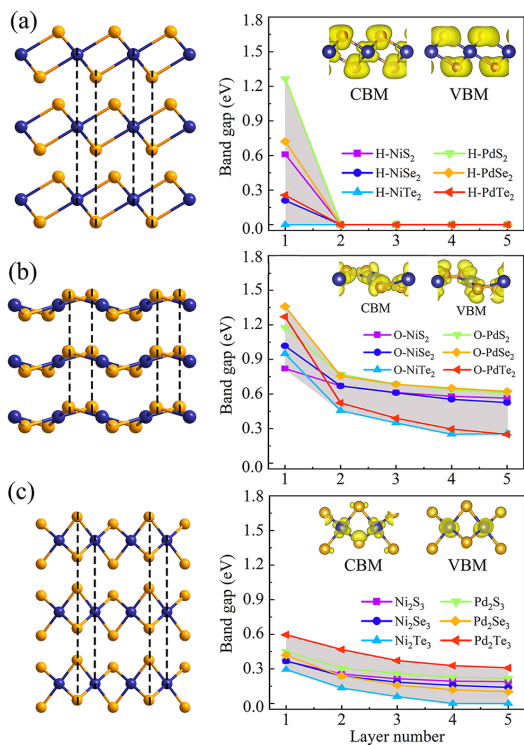


FIG. 5. Atomic structures of few-layer TMCs and layer number-dependent PBE band gaps for (a) H-MX₂, (b) O-MX₂ and (c) O-M₂X₃, respectively. The insets are band-decomposed charge densities of monolayer H-NiS₂, O-NiS₂ and Ni₂S₂ for CBM and VBM, respectively.

band minimum (CBM) and the valence band maximum (VBM) are mainly attributed from element X; for O-MX₂ and O-M₂X₃ phases, the CBM and VBM originate from both compounds of M and X. The values of band gap ob-

tained from both PBE and HSE06 are listed in Table 1. It indicates that for the materials in the same structural phase, the band gaps always decrease as the element X varies from S to Te, which are similar to those observed in MoX₂ and WX₂ (X=S, Se and Te) [51]. As there are relatively heavy elements in the considered TMCs, it is worth checking also the effects of the SOC. From the results obtained with or without SOC in PBE (see details in Supplementary Information), the SOC interaction is overall negligible for most materials considered in our paper, except H-PdSe₂ and H-PdTe₂. In these two materials, there are large splittings of energy bands due to SOC, especially around the Γ points. However, these splitting will not change qualitatively the properties we are interested in (see details in Fig. S7), therefore we will mainly show results without SOC in the following.

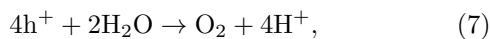
All three phases of TMCs present stable multilayer structures stacked along the direction perpendicular to their plane. In Fig. 5(a), we show atomic structures of stacked trilayer TMCs. The stacking sequence of H-MX₂, O-MX₂ and O-M₂X₃ is AAA stacking. We calculate further the electronic properties of multilayer TMCs by using relaxed structures as shown in Fig. 5(a), and present the main results in Fig. 5(b). Here, we consider mainly the thickness-dependence of the electronic properties of multilayer structure, and show the values of band gap with different number of layers ranging from 1 to 5. As is well known, the interlayer vdW interaction, which is absent in a monolayer, plays a vital role to determine the properties of multilayer 2D materials, especially at low energy around the Fermi level. In general, the interlayer vdW interaction will lower the band gap for semi-conducting 2D materials, because of the hybridization of the bands between neighboring layers. This is indeed also the case for TMCs considered in our paper. In particular, once H-MX₂ becomes a bilayer, its band gap promptly

decreases to zero (see the results shown in Fig. S8), indicating that it gives a fierce response to the thickness. For O-MX₂ and O-M₂X₃ phases, their band gaps keep decreasing when adding more layers, but slowly. Specifically, the variation ranges of band gaps are 0 ~ 1.27 eV, 0.26 ~ 1.36 eV and 0 ~ 0.60 eV for H-MX₂, O-MX₂ and O-M₂X₃, respectively. To further explore the origin of the relationship between the band gaps and the inter-layer coupling, Fig. 5 shows the band decomposed charge densities of CBM and VBM in the monolayer. For H-NiS₂, O-NiS₂ and O-Ni₂S₃, charge densities of CBM and VBM are distributed among outside S atoms, Ni-S bonds and inside Ni atoms, respectively. When the monolayers are stacked together, the few-layer H-NiS₂ and O-Ni₂S₃ have maximum (minimum) interlayer charge overlapping, leading to maximum (minimum) change of band gap.

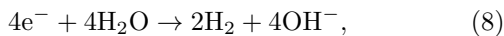
D. Photocatalyst and light absorption

Most monolayer TMCs considered in this paper are semiconducting with energy gaps ranging from 0.52 to 2.40 eV according to HSE06 calculations, providing a wide range of candidates for different optical applications. The main concern in the following is to study their potential applications in the photocatalytic water splitting, *i.e.*, converting the solar energy into the chemical energy without additional cost [21–24]. As designing principles, a highly efficient water splitting photocatalyst should hold two characters: (i) a band gap about 2.0 eV for the harvest of the solar energy ; (ii) the band edges (CBM and VBM) must straddling both the reduction potential of H₂/H⁺ (-4.44 eV, pH=0) and the oxidation potential of H₂O/O₂ (-5.67 eV, pH=0). Here the hydrogen production via photocatalytic water splitting needs ultrahigh solar energy harvest to drive the oxidation and reduction reactions.

To be more precise, in the oxidation reaction, the holes are used to generate O₂:



meanwhile, the excited electrons take part in the hydrogen reduction reaction to produce H₂:



In fact, the redox potentials of water are related to the pH of aqueous solution. According to the Nernst equation [52–54], the water redox potentials and the value of pH satisfy the following relation:

$$E^{pH} = E^{pH=0} - 0.059 \times pH, \quad (9)$$

which means that, the redox potentials of water increase linearly with pH by a factor of 0.059eV/pH.

Here, in Fig. 6, by adopting HSE06 method, the accurate band alignments of monolayer TMCs are obtained. For the H-MX₂ phase, the CBM and VBM never meet

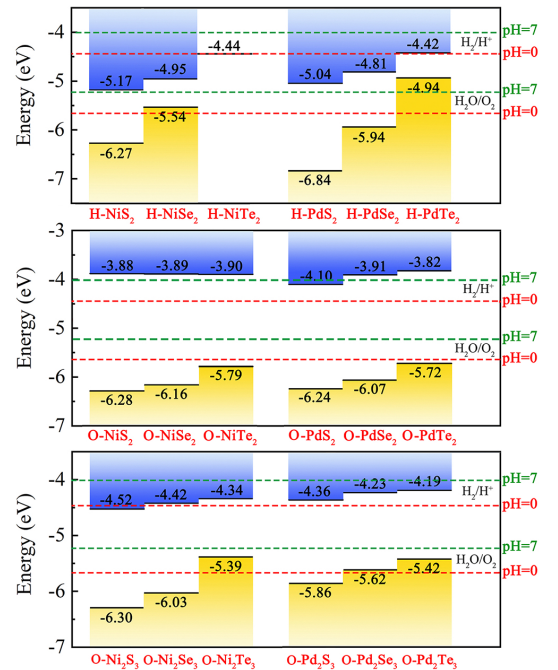


FIG. 6. Band alignments of monolayer H-MX₂, O-MX₂ and O-M₂X₃ with respect to the redox potentials of water.

the requirement of redox potentials at pH=0 or 7, indicating that they can not be used for achieving water splitting. For the O-MX₂ phase, the CBM and VBM are always higher and lower than the reduction and oxidation potentials at pH=0, respectively, implying that they have inherent advantage in realizing water splitting. When the pH of aqueous solution increases to 7, only the CBM of monolayer O-PdS₂ fails in producing H₂. For the O-M₂X₃ phase, both O-Ni₂Se₃ and O-Pd₂S₃ meet the redox potentials at pH=0, but they fail in realizing water splitting at pH=7. To further analysis the ability of water splitting, the kinetic overpotentials ΔE_C and ΔE_V (the difference between band edge and redox potential) are tested, which can represent properly the efficiency of driving the redox reaction (see details in Table S2 of the Supplementary Information). It shows that when pH of aqueous solution increases, ΔE_C decreases and ΔE_V increases. The pH value-dependent kinetic overpotential shows tunable ability of H₂ production. These results imply that O-MX₂, O-Ni₂Se₃ and O-Pd₂S₃ are possible photocatalysts for water splitting at specific pH of aqueous solution.

To investigate the actual performance, we need further consider the sunlight harvest of these candidates by calculating optical absorption coefficients. Using the GW approximation in conjunction with the Bethe-Salpeter equation (BSE) [56, 57], the light absorbance is obtained and plotted in Fig. 7. Here we include the electron-hole interaction in the optical calculation, as the charge screening effect is much weaker in two-dimension comparing to three-dimension due to the absence of screen-

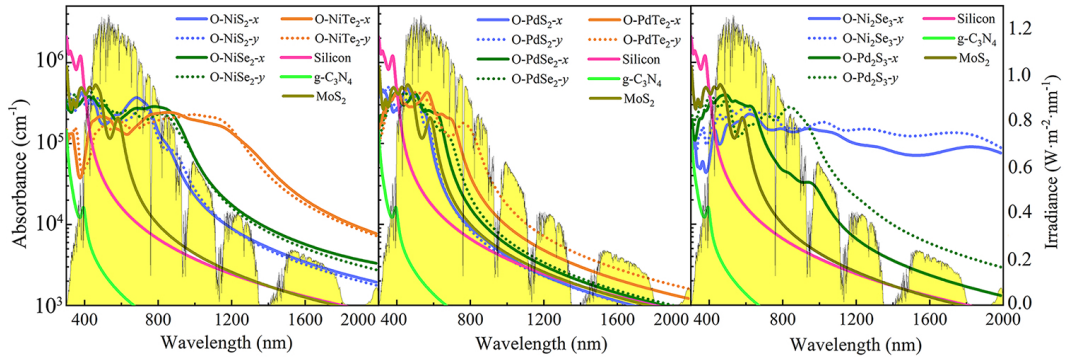


FIG. 7. The absorption coefficients of monolayer O-MX₂ phase, O-Ni₂Se₃ and O-Pd₂S₃, respectively, calculated with GW-BSE. The yellow background denotes the reference solar spectral irradiance in incident AM1.5G solar flux [55].

ing along the out-of-plane direction. The solar energy is distributed in the infrared, visible and ultraviolet light about 43%, 50% and 7%, respectively. Fig. 7 shows that O-MX₂, O-Ni₂Se₃ and O-Pd₂S₃ have ultrahigh absorption coefficients within both visible (400-760 nm) and ultraviolet ranges (<760 nm), indicating their excellent harvest of the solar energy. As a comparison, we perform optical calculations of widely used intrinsic silicon, and other 2D semiconductor photocatalysts, including g-C₃N₄ and MoS₂. When the wavelength is longer than 400 nm, the absorption coefficients of our TMCs candidates are much higher than all other compared materials, for example, about ten times higher than the value of intrinsic silicon. specially, O-Ni₂Se₃ shows high and constantly absorption over the entire energy range of the sunlight. Our results identify that O-MX₂, O-Ni₂Se₃ and O-Pd₂S₃ have large absorption coefficients from visible to ultraviolet light and provide congenital advantages for applications as photocatalyst. Furthermore, monolayer O-MX₂, O-Ni₂Se₃ and O-Pd₂S₃ present highly anisotropic optical properties, consistent with their mechanical properties. These materials can be used also for polarization-dependent photodetectors, similar as these proposed for other 2D materials such as black phosphorus [58].

IV. CONCLUSIONS

In conclusion, we have studied three phases of monolayer transition metal chalcogenides H-MX₂, O-MX₂ and

O-M₂X₃ (M= Ni, Pd; X= S, Se, Te). We systematically examined their structural, mechanical and electronic characteristics via first-principle calculations. All these structures are stable at room temperature, verified by time-dependent ab initio molecular dynamics simulations and their phonon dispersion. The calculated mechanical properties also show that H-MX₂ is isotropic, while O-MX₂ and O-M₂X₃ present highly in-plane anisotropy due to their reduced lattice symmetry. Furthermore, O-MX₂ shows great auxeticity with giant negative in-plane Poisson's ratios, which are comparable to other known two-dimensional materials. Hence, O-MX₂ has ultra-low Young's modulus. By calculating the band alignments and light absorption coefficients, we concluded that O-MX₂, O-Ni₂Se₃ and O-Pd₂S₃ can be used as flexible water splitting photocatalysts within visible and ultraviolet light regions, because of their suitable band gaps, band edges and ultrahigh sunlight absorption.

ACKNOWLEDGEMENTS

This work is supported by the National Key R&D Program of China (Grant No. 2018FYA0305800). Numerical calculations presented in this paper have been performed on a supercomputing system in the Supercomputing Center of Wuhan University.

-
- [1] B. Radisavljevic, A. Radenovic, J. Brivio, V. Giacometti, and A. Kis, *Nat. Nanotechnol.* **6**, 147 (2011).
 - [2] Q. H. Wang, K. Kalantar-Zadeh, A. Kis, J. N. Coleman, and M. S. Strano, *Nat. Nanotechnol.* **7**, 699 (2012).
 - [3] O. Lopez-Sanchez, D. Lembke, M. Kayci, A. Radenovic, and A. Kis, *Nat. Nanotechnol.* **8**, 497 (2013).
 - [4] F. H. L. Koppens, T. Mueller, P. Avouris, A. C. Ferrari, M. S. Vitiello, and M. Polini, *Nat. Nanotechnol.* **9**, 780 (2014).
 - [5] K. F. Mak, K. He, J. Shan, and T. F. Heinz, *Nat. Nanotechnol.* **7**, 494 (2012).
 - [6] H. Zeng, J. Dai, W. Yao, D. Xiao, and X. Cui, *Nat. Nanotechnol.* **7**, 490 (2012).
 - [7] L. Li, Y. Yu, G. J. Ye, Q. Ge, X. Ou, H. Wu, D. Feng, X. H. Chen, and Y. Zhang, *Nat. Nanotechnol.* **9**, 372 (2014).

- [8] J. Qiao, X. Kong, Z.-X. Hu, F. Yang, and W. Ji, *Nat. Commun.* **5**, 4475 (2014).
- [9] L. C. Gomes and A. Carvalho, *Phys. Rev. B* **92**, 085406 (2015).
- [10] P. Z. Hanakata, A. Carvalho, D. K. Campbell, and H. S. Park, *Phys. Rev. B* **94**, 035304 (2016).
- [11] L. Xu, M. Yang, S. J. Wang, and Y. P. Feng, *Phys. Rev. B* **95**, 235434 (2017).
- [12] H. Tian, J. Tice, R. Fei, V. Tran, X. Yan, L. Yang, and H. Wang, *Nano Today* **11**, 763 (2016).
- [13] L. Kou, C. Chen, and S. C. Smith, *J. Phys. Chem. Lett.* **6**, 2794 (2015).
- [14] X. Wang, A. M. Jones, K. L. Seyler, V. Tran, Y. Jia, H. Zhao, H. Wang, L. Yang, X. Xu, and F. Xia, *Nat. Nanotechnol.* **10**, 517 (2015).
- [15] E. Li, D. Wang, P. Fan, R. Zhang, Y.-Y. Zhang, G. Li, J. Mao, Y. Wang, X. Lin, S. Du, and H.-J. Gao, *Nano Res.* **11**, 5858 (2018).
- [16] W. L. Chow, P. Yu, F. Liu, J. Hong, X. Wang, Q. Zeng, C.-H. Hsu, C. Zhu, J. Zhou, X. Wang, J. Xia, J. Yan, Y. Chen, D. Wu, T. Yu, Z. Shen, H. Lin, C. Jin, B. K. Tay, and Z. Liu, *Adv. Mater.* **29**, 1602969 (2017).
- [17] L.-H. Zeng, D. Wu, S.-H. Lin, C. Xie, H.-Y. Yuan, W. Lu, S. P. Lau, Y. Chai, L.-B. Luo, Z.-J. Li, and Y. H. Tsang, *Adv. Funct. Mater.* **29**, 1806878 (2019).
- [18] A. D. Oyedele, S. Yang, L. Liang, A. A. Puzdov, K. Wang, J. Zhang, P. Yu, P. R. Pudasaini, A. W. Ghosh, Z. Liu, C. M. Rouleau, B. G. Sumpter, M. F. Chisholm, W. Zhou, P. D. Rack, D. B. Geohegan, and K. Xiao, *J. Am. Chem. Soc.* **139**, 14090 (2017).
- [19] G. D. Nguyen, L. Liang, Q. Zou, M. Fu, A. D. Oyedele, B. G. Sumpter, Z. Liu, Z. Gai, K. Xiao, and A.-P. Li, *Phys. Rev. Lett.* **121**, 086101 (2018).
- [20] J. Lin, S. Zuluaga, P. Yu, Z. Liu, S. T. Pantelides, and K. Suenaga, *Phys. Rev. Lett.* **119**, 016101 (2017).
- [21] A. Iwase, Y. H. Ng, Y. Ishiguro, A. Kudo, and R. Amal, *J. Am. Chem. Soc.* **133**, 11054 (2011).
- [22] K. Maeda and K. Domen, *J. Phys. Chem. Lett.* **1**, 2655 (2010).
- [23] P. Wang, B. Huang, X. Qin, X. Zhang, Y. Dai, J. Wei, and M.-H. Whangbo, *Angew. Chem., Int. Ed.* **47**, 7931 (2008).
- [24] A. Fujishima and K. Honda, *Nature* **238**, 37 (1972).
- [25] Q. Lu, Y. Yu, Q. Ma, B. Chen, and H. Zhang, *Adv. Mater.* **28**, 1917 (2016).
- [26] Y. Zhang, J. Liu, G. Wu, and W. Chen, *Nanoscale* **4**, 5300 (2012).
- [27] G. Kresse and J. Furthmüller, *Phys. Rev. B* **54**, 11169 (1996).
- [28] P. E. Blöchl, *Phys. Rev. B* **50**, 17953 (1994).
- [29] J. P. Perdew, K. Burke, and M. Ernzerhof, *Phys. Rev. Lett.* **77**, 3865 (1996).
- [30] H. J. Monkhorst and J. D. Pack, *Phys. Rev. B* **13**, 5188 (1976).
- [31] S. Grimme, *J. Comp. Chem.* **27**, 1787 (2006).
- [32] T. Kerber, M. Sierka, and J. Sauer, *J. Comp. Chem.* **29**, 2088 (2008).
- [33] J. Heyd, J. E. Peralta, G. E. Scuseria, and R. L. Martin, *J. Chem. Phys.* **123**, 174101 (2005).
- [34] X. Gonze, J.-C. Charlier, D. Allan, and M. Teter, *Phys. Rev. B* **50**, 13035 (1994).
- [35] X. Gonze and C. Lee, *Phys. Rev. B* **55**, 10355 (1997).
- [36] P. Giannozzi, S. de Gironcoli, P. Pavone, and S. Baroni, *Phys. Rev. B* **43**, 7231 (1991).
- [37] J. D. Gale and A. L. Rohl, *Mol. Simulat.* **29**, 291 (2003).
- [38] J. D. Gale, *J. Chem. Soc., Faraday Trans.* **93**, 629 (1997).
- [39] J. Zhou, J. Lin, X. Huang, Y. Zhou, Y. Chen, J. Xia, H. Wang, Y. Xie, H. Yu, J. Lei, D. Wu, F. Liu, Q. Fu, Q. Zeng, C.-H. Hsu, C. Yang, L. Lu, T. Yu, Z. Shen, H. Lin, B. I. Yakobson, Q. Liu, K. Suenaga, G. Liu, and Z. Liu, *Nature* **556**, 355 (2018).
- [40] Y. Shao, S. Song, X. Wu, J. Qi, H. Lu, C. Liu, S. Zhu, Z. Liu, J. Wang, D. Shi, S. Du, Y. Wang, and H.-J. Gao, *Appl. Phys. Lett.* **111**, 113107 (2017).
- [41] P. Miró, M. Ghorbani-Asl, and T. Heine, *Angew. Chem., Int. Ed.* **53**, 3015 (2014).
- [42] H. Zhong, K. Huang, G. Yu, and S. Yuan, *Phys. Rev. B* **98**, 054104 (2018).
- [43] V. Wang and W. T. Geng, *J. Phys. Chem. C* **121**, 10224 (2017).
- [44] C. Lee, X. Wei, J. W. Kysar, and J. Hone, *Science* **321**, 385 (2008).
- [45] D. Çakır, F. M. Peeters, and C. Sevik, *Appl. Phys. Lett.* **104**, 203110 (2014).
- [46] Z. Gao, X. Dong, N. Li, and J. Ren, *Nano Lett.* **17**, 772 (2017).
- [47] S. Zhang, J. Zhou, Q. Wang, X. Chen, Y. Kawazoe, and P. Jena, *Proc. Natl. Acad. Sci.* **112**, 2372 (2015).
- [48] Y. Wang, F. Li, Y. Li, and Z. Chen, *Nat. Commun.* **7**, 11488 (2016).
- [49] W.-Z. Xiao, G. Xiao, Q.-Y. Rong, and L.-L. Wang, *Phys. Chem. Chem. Phys.* **20**, 22027 (2018).
- [50] L.-C. Zhang, G. Qin, W.-Z. Fang, H.-J. Cui, Q.-R. Zheng, Q.-B. Yan, and G. Su, *Sci. Rep.* **6**, 19830 (2016).
- [51] J. Kang, S. Tongay, J. Zhou, J. Li, and J. Wu, *Appl. Phys. Lett.* **102**, 012111 (2013).
- [52] J. M. Bolts and M. S. Wrighton, *J. Phys. Chem.* **80**, 2641 (1976).
- [53] X. Li, J. Yu, J. Low, Y. Fang, J. Xiao, and X. Chen, *J. Mater. Chem. A* **3**, 2485 (2015).
- [54] T. A. Pham, D. Lee, E. Schwegler, and G. Galli, *J. Am. Chem. Soc.* **136**, 17071 (2014).
- [55] G. Committee, *ASTM International*, DOI: 10.1520/G0173 (2008).
- [56] M. Rohlfing and S. G. Louie, *Phys. Rev. B* **62**, 4927 (2000), 50.
- [57] J. Deslippe, G. Samsonidze, D. A. Strubbe, M. Jain, M. L. Cohen, and S. G. Louie, *Comput. Phys. Commun.* **183**, 1269 (2012).
- [58] Q. Guo, A. Pospischil, M. Bhuiyan, H. Jiang, H. Tian, D. Farmer, B. Deng, C. Li, S.-J. Han, H. Wang, Q. Xia, T.-P. Ma, T. Mueller, and F. Xia, *Nano Lett.* **16**, 4648 (2016).